Aeroacoustics Conferences
June 4-7, 2024, Rome, Italy
30th AIAA/CEAS Aeroacoustics Conference (2024)

10.2514/6.2024-3266

Towards a controlled roughness for improved aerodynamic and acoustic performance of propellers at low Reynolds number

Yoann Beausse * and Benjamin Cotté †
IMSIA, ENSTA Paris, Institut Polytechnique de Paris, Palaiseau, France

Caroline Pascal ‡
U2IS, ENSTA Paris, Institut Polytechnique de Paris, Palaiseau, France

The influence of roughness on the aerodynamic and acoustic performances of propellers at low Reynolds numbers is studied, both with models and experimentally. Three propellers with different manufacturing methods are studied (wood, PLA, VeroWhite), and slight experimental differences are shown, like an increase of broadband noise for the wooden propeller (lowest roughness levels) and a decrease of lift for the PLA propeller (highest roughness levels). The numerical models are validated against experimental measurements, and these models are used to obtain the evolution of the boundary layer parameters along the chord. A laminar separation bubble is spotted on the suction side. Ideas for the design of an improved propeller with controlled roughness are discussed.

I. Introduction

The global increase in the number of unmanned aerial vehicles is a major trend in the last few years, for military and civil applications [1]. In particular, their multiplication in urban settings has called for a better understanding of the noise emissions of their propellers, given that rotor diameters can be significantly smaller than aircraft propeller diameters. For low Reynolds numbers (less than 10^6), the question of the transition (or not) to turbulence in the boundary layers is often present, with laminar boundary layers typically associated with tonal trailing-edge noise, when a turbulent boundary layer is associated with broadband trailing-edge noise [2–4]. A change in surface roughness on a wing or a propeller can have an influence on the boundary layer behaviour, notably on its laminar-turbulent transition via the formation of a laminar separation bubble, as can be seen in the work of Jaroslawski et al. [5]. In addition to its impact on lift and drag forces, the boundary layer regime also influences the acoustic emissions emitted by a wing profile [3].

The main objective of this work is to study the influence of surface roughness on the aerodynamic and aeroacoustic properties of a propeller, and to advance in the search towards a better propeller design in terms of reduction of noise and aerodynamic performance. To this effect, the first part is an experimental campaign (acoustic and aerodynamic measurements) using the same geometry for the production of multiple propellers of variable surface roughness, made with different techniques and materials. Then, numerical modeling of the system via Blade Element Momentum Theory (BEMT) coupled to a panel method [6, 7] and Hanson model for steady loading noise [8] will allow a better understanding of the phenomena. Finally, an improved design (that can include a trip or other roughness apparatus) will be discussed.

II. Materials and methods

A. Experimental apparatus

The experimental bench presented here derives from the DLR small-scale rotor benchmark presented by Yin et al. [9]. Placed inside an anechoic chamber, the test rig is made of a vertical aluminum pole on which a 6-axis thrust and torque sensor (ATI Mini40), an engine and a propeller (XOAR 13x7 propeller) are mounted. Two different engines are used, a first one (Faulhaber 3274 series) limited to a maximum of 5000 rotations per minute (RPM), and a second one bought during the experiments (Faulhaber 4490 series) reaching 6000 RPM. So the rotation speeds vary between 1000 and 6000 RPM, leading to Reynolds numbers (at 80% of the tip, and based on the chord) between 10^4 and 10^5. A

*Postdoctoral researcher, ENSTA Paris, Institute of Mechanical Sciences and Industrial Applications, yoann.beausse@ensta-paris.fr
†Assistant professor, ENSTA Paris, Institute of Mechanical Sciences and Industrial Applications
‡PhD student, ENSTA Paris, Unité d'Informatique et d'Ingénierie des Systèmes

picture of the bench is presented in Figure 1, exhibiting the bench and the 7-axis robotic arm (Franka Emika Panda) used for handling and positioning the microphone. For most of the measurements afterwards, the microphone is set in an arc of a circle around the propeller with a radius of 30 cm, orthogonal to the plane of the rotor. The positions are set with Θ, the angle on the arc between the microphone and the plane of the rotor : Θ = [-60°,-45°,-30°,-15°,0°,15°,30°]. Another circular arc is used, R = 0.7m with Θ = [-30°,-20°... until +60°].

All three propellers share the same geometry, a XOAR 13x7 propeller (PJN Series) with a diameter of 33.02 cm that has been scanned by DLR. The model for the scan was made of varnished wood and is the first propeller used here. The second is made of PLA (PolyLactic Acid) and produced by classical filament-based 3D-printing. The third one is made of VeroWhite and produced by another 3D-printing technique called polyjet printing. Pictures of the propellers are shown in Figure 1.

Fig. 1 Pictures of the experimental bench in the anechoic room (left) and of the propellers (right). From top to bottom, VeroWhite propeller, PLA propeller, wood propeller.

Roughness levels are measured on each propeller using a skidless roughness tester (Someco RTP80-TL9), and are presented in Figure 2. Surface roughness widely differs between propellers. These differences can be objectively assessed with a parameter called Ra, the average deviation of the roughness profile. This parameter is 19.6 µm for the PLA propeller, 5.5 µm for the VeroWhite propeller and 1.0 µm for the wood propeller.

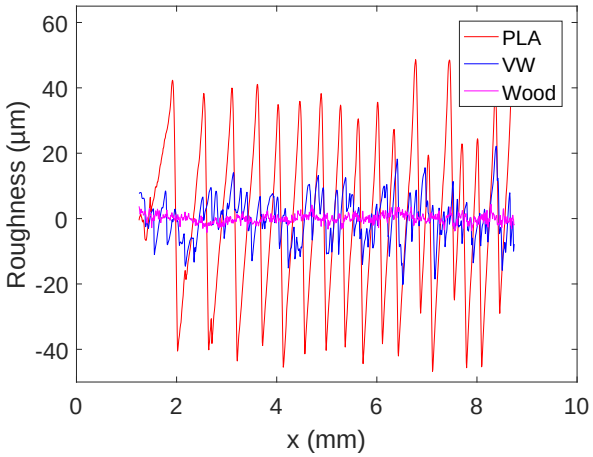

Fig. 2 Roughness levels measured along the chord on each propeller.

B. Aerodynamic and acoustic modeling

1. Blade Element Momentum Theory

The chord and twist of the propeller used in our experiments along the radial dimension are known [9]. In order to use Blade Element Momentum Theory (BEMT) [6, 7, 10], lift and drag coefficients are needed on each sectional aerofoil section. These sections are approximated by using three different profiles. A first profile is chosen between $r = 0$ and $r = 0.6r_{tip}$ (zone 1, NACA 6420), a second one between $r = 0.6r_{tip}$ and $r = 0.84r_{tip}$ (zone 2, NACA 5416), and a third one between $r = 0.84r_{tip}$ and $r = r_{tip}$ (zone 3, NACA 3417). This division is shown in Figure 3. The approximations are 4-digits NACA profiles, and are chosen with the camber and the thickness of the propeller on the corresponding position. These parameters are evaluated for some sections, via a 3D scan of the propeller. The wing is only simulated between $r = 0.21r_{tip}$ and $r = 0.95r_{tip}$, $0.21r_{tip}$ being the position of the end of the central hub of the propeller and $r = 0.95r_{tip}$ being the position of the last scanning slice of the propeller.

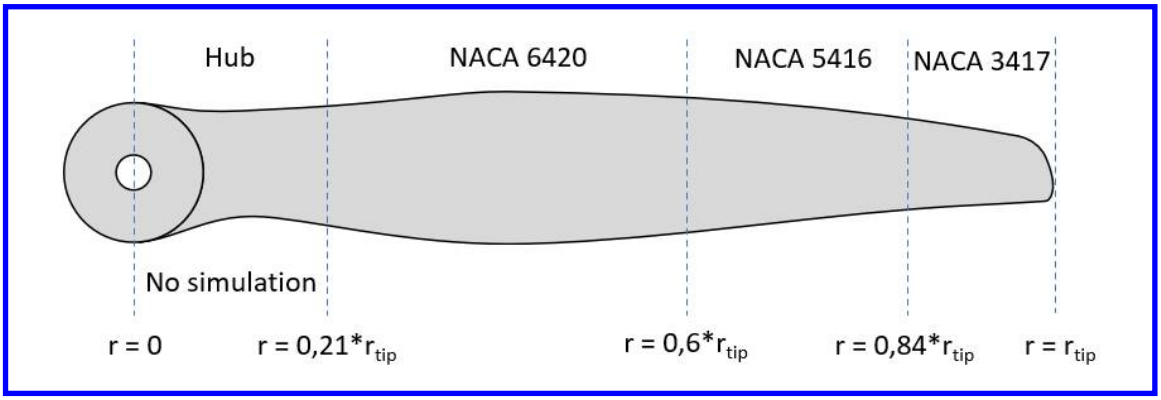

Fig. 3 Division of the propeller in regions for approximation as NACA profiles. It is not shown here for readability, but the part between $0.95r_{tip}$ and r_{tip} is not simulated.

The BEMT is used with corrections in order to take into account the effect of the hub [6] and the tip vortex [6, 10]. A three-dimensional flow correction is also implemented [10].

For each profile, the lift and drag coefficients are calculated using XFOIL, for multiple Reynolds numbers. The calculation from XFOIL is only the first part of the curve, from -5 degrees to the stall incidence. Above the stall incidence, XFOIL does not compute consistent results anymore. The second part of the curve is an extension for high angle-of-attack coefficients, using a method developed by Viterna and Corrigan [11]. The change of method is shown on Figure 4, where the coefficients of lift and drag are calculated for typical Reynolds numbers for each zone on the blade : 60,000 in zone 1, 100,000 in zone 2 and 85,000 in zone 3. It appears that the curves of lift and drag for the NACA 5416 and NACA 3417 profiles are close to each other, while the NACA 6420 stands out. With this thicker and more curved profile, the stall angle seems to be extremely high, distorting the shape of the curves.

For a chosen rotation rate, the BEMT algorithm uses the curves of lift and drag coefficients to converge on a flow velocity and angle, for each radial position. These BEMT aerodynamic results are plotted in Fig. 5, using the same definition and name of variables as Ning [6]. Both the local angle of attack α and induced velocity u have a consistent and mainly continuous evolution along the radius of the propeller (only little discontinuities appear at $r = 0.6 * r_{tip}$ and $r = 0.84 * r_{tip}$, when the approximated NACA profile changes).

When comparing the Figures 4 and 5, it appears that the local angle of attack used on the final iteration of the BEMT algorithm is never obtained via the high angle-of-attack extrapolation. Most radial positions have a pitch between 5 degrees and 13 degrees, corresponding to relatively high values of lift and low values of drag on Fig. 4. These values of local angle of attack and induced velocity are used in part III.C for the boundary layer analysis.

2. Loading noise

The method used here to predict the steady loading noise is the frequency-domain model proposed by Hanson and Parzych [8]. The equations for the thickness noise and quadrupole noise from the article have not been added to our model, only the steady loading noise part. The local distribution of forces on the propeller is predicted with the BEMT algorithm, and this prediction is used as an entry parameter for the loading noise prediction. The radius of the propeller

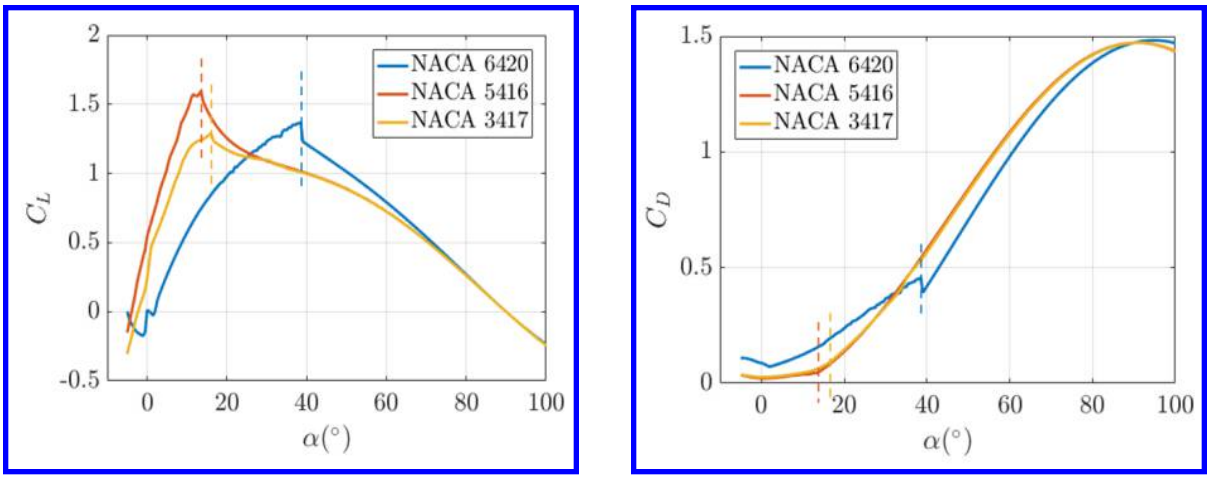

Fig. 4 Lift and drag coefficients for each NACA profile. The Reynolds number is chosen according to the position of each profile on the propeller, here for 6000 RPM : Re = 60,000 for the NACA 6420, Re = 100,000 for the NACA 5416, Re = 85,000 for the NACA 3417. The dotted lines show the delimitation between the XFOIL results (on the left) and the high angle-of-attack extrapolation (on the right).

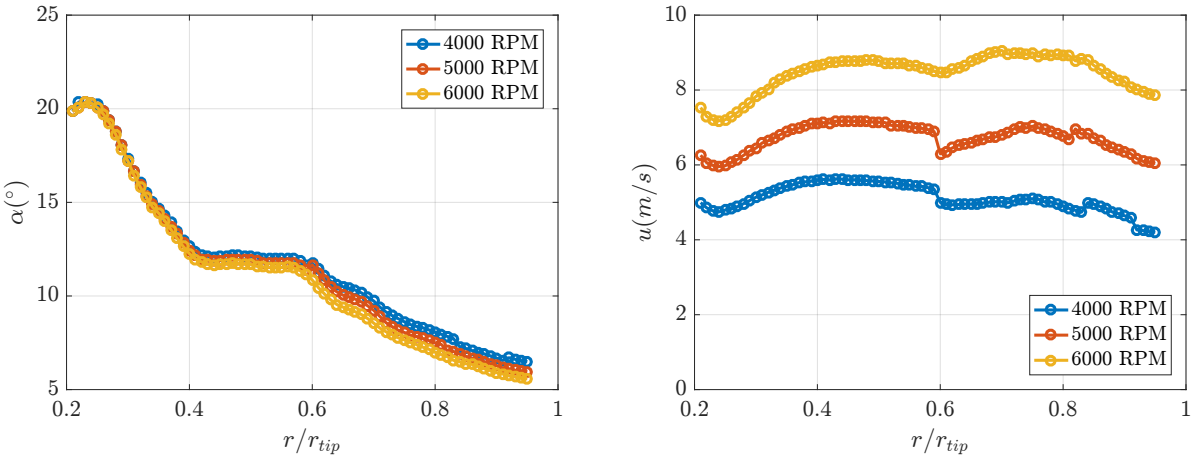

Fig. 5 BEMT aerodynamic results for the XOAR 13x7 at 6000 RPM : local angle of attack α (on the left) and induced velocity u (on the right).

is discretized in 79 elements, with only one element along the chord dimension. This model includes a far field and a near field prediction (the latter taking into account near field effects).

In Fig. 6, the predicted spectrum levels are plotted, for two angular positions on the arc R = 0.3 m, and a rotation rate of 6000 RPM. The near field prediction is always higher than the far field prediction, and this difference is larger for the case far from the rotor plane ($\theta = -45°$). As will be shown in Part III.B, the near field model provides a better prediction than the far field model for any of our distances, especially on the main peak (f = BPF).

As the height of the main peak is the part of the spectrum that is the most accurately predicted, it is now chosen instead of the spectrum as a point of comparison in Fig. 7, for different rotation rates and angles. On these directivity plots, the near field model appears once again to be always noticeably higher than the far field model. For the rest of the article, the near field model is preferred and the far field model will not be used again.

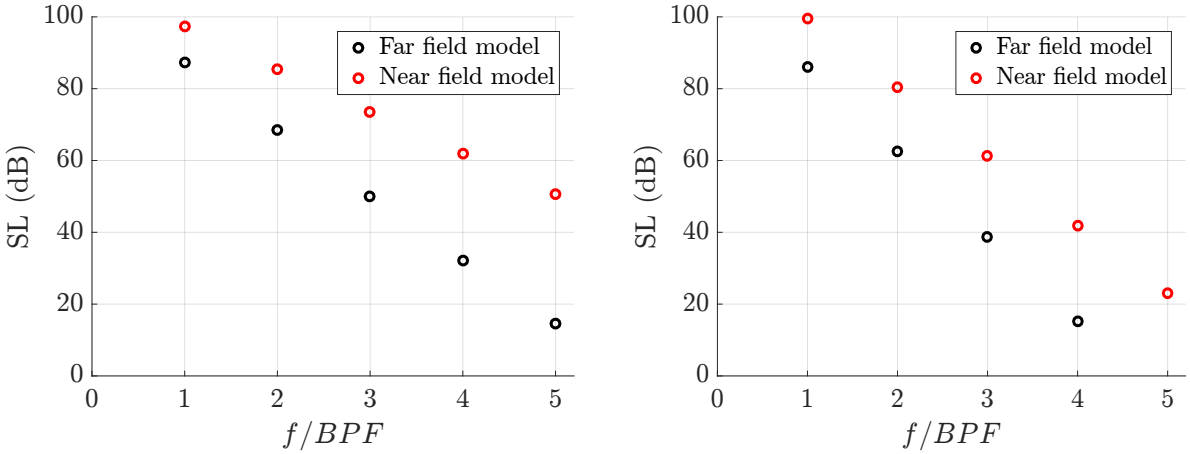

Fig. 6 Predicted spectrum levels (SL) for the near field and far field models for loading noise. 6000 RPM, Θ = 0° (left) or Θ = -45° (right), R = 0.3 m.

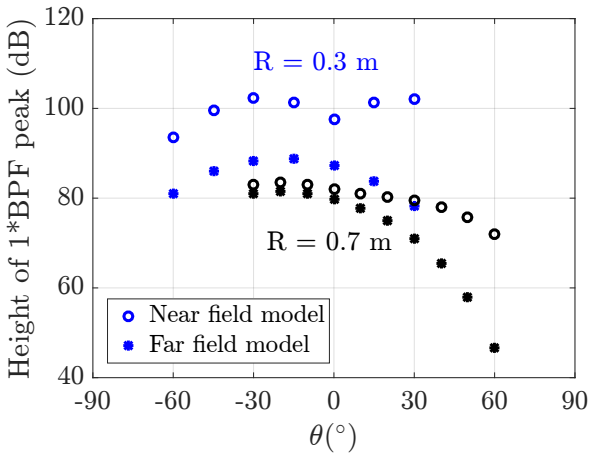

Fig. 7 Directivity figure for the far field and near field models for loading noise. 6000 RPM.

III. Results and discussion

A. Effect of rugosity

The two main efforts measured with our thrust and torque sensor are the vertical thrust of the propeller (F_Z) and the torque (M_Z), plotted in Figure 8 for each propeller as a function of the rotation speed, with a comparison to the results of Yin et al [9] for the wooden propeller.

Both the thrust and the torque agree well with the results of Yin et al [9] at 2000 and 4000 RPM. As explained in part II.A, the engine used at the beginning of the experiments was limited to 5000 RPM, and so only the wooden propeller has been tested at 6000 RPM with the new engine. The results at 6000 RPM are once again consistent with Yin et al. Some differences appear between propellers : the PLA propeller (highest roughness levels) stands out, with a lower thrust and a lower torque (in absolute value).

The Spectrum Level (SL) of the tonal noise emitted by each propeller is presented for two microphone positions in Figure 9, as a function of the frequency divided by the Blade Passing Frequency (BPF). The main peaks displayed are multiples of this BPF, with peaks of lower amplitude on multiples of 0.5*BPF. The amplitude of the main peaks looks similar for each propeller, while the secondary peaks are notably different, with higher amplitudes for the VeroWhite propeller. This could be due to imbalance. On the position Θ = -45°, it can also be noted that the broadband noise is notably more powerful for the wooden propeller.

To better investigate potential differences on the two main peaks (f = BPF and f = 2*BPF), we plot only the amplitude

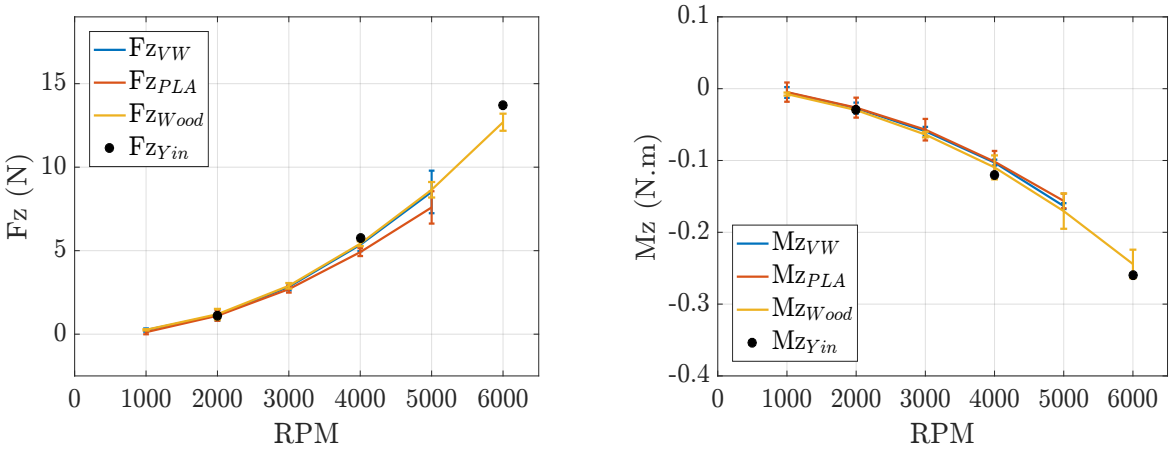

Fig. 8 Experimental measurements of thrust and torque as a function of rotation speed and propeller. The black dots show the results of Yin et al. [9].

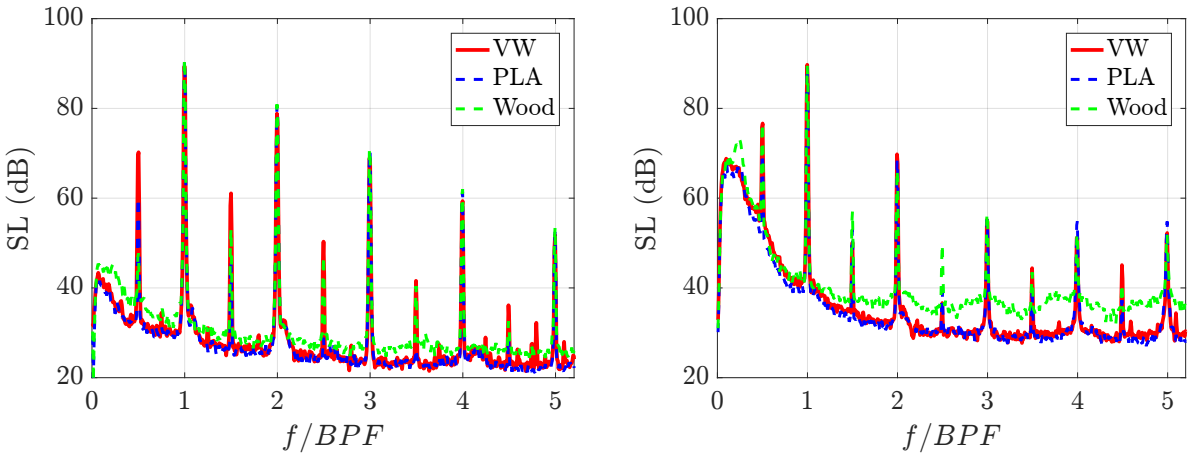

Fig. 9 Spectrum Levels (SL) for each propeller. 4000 RPM, Θ = 0° (left) or Θ = -45° (right).

of these peaks for different positions of the microphones in Figure 10. The amplitudes of the main peaks are still close regardless of the propeller, and the directivity curves show the same behaviour. However, a closer examination shows that the amplitudes are slightly lower for the PLA propeller than the others, except for Θ = 0° and Θ = 15°.

The broadband part of the spectrum is presented in Figure 11, showing the frequencies between 6*BPF = 800 Hz and 20 kHz. The levels are overall much higher at Θ = -45° than at Θ = 0°, which is consistent with the trailing-edge noise directivity. The acoustic emissions from the wooden propeller (lowest roughness levels) exceed the others, with then the VeroWhite propeller and finally the PLA (highest roughness levels). This increase in broadband emissions for the wooden propeller is more marked at Θ = -45°.

Moreover, a spectral hump appear at Θ = 0° around 1.8 kHz on the VeroWhite propeller. This frequency is much higher than the BPF, but the phenomenon is tonal.

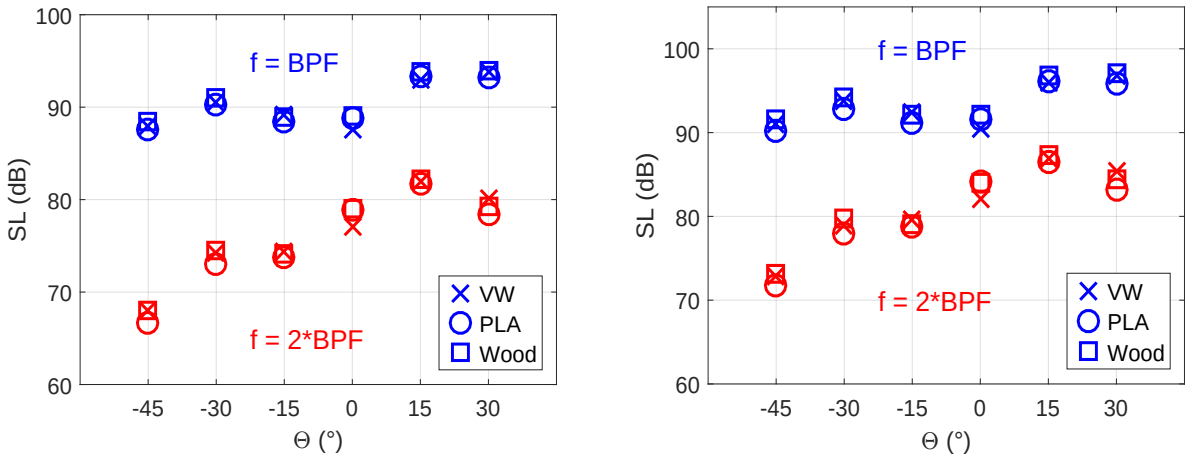

Fig. 10 Main peaks amplitude for each propeller, as a function of the microphone position. Rotational speed of 4000 RPM (left) and 5000 RPM (right), R = 0.3m.

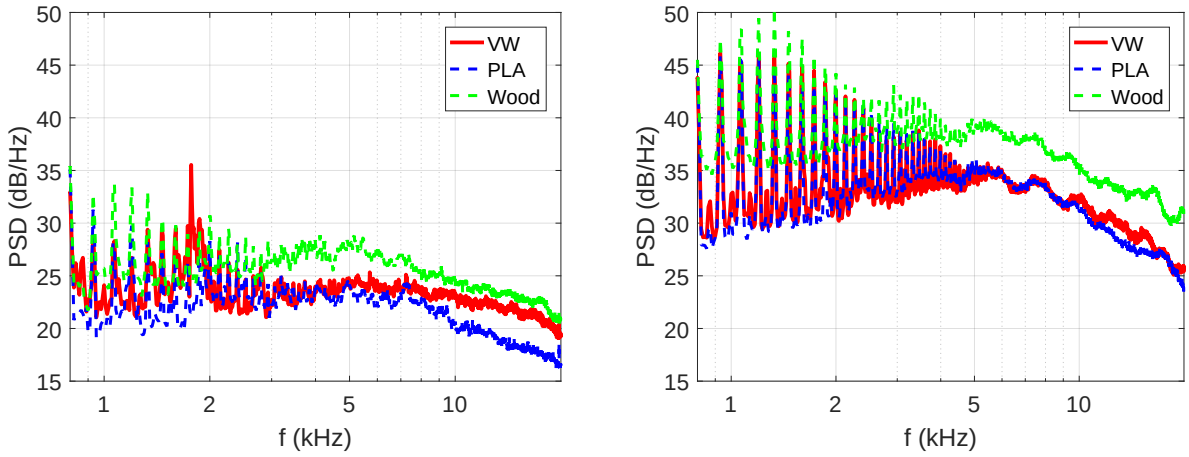

Fig. 11 Power Spectral Density (PSD) for each propeller, for frequencies between 6*BPF and 20 kHz. 4000 RPM, Θ = 0° (left) or Θ = -45° (right).

B. Validation of the numerical model on the wooden propeller

The numerical model is tested against reference values from Yin et al. [9] and experimental values on the wooden propeller, the one with the lower surface rugosity levels. The results are shown in Figure 12. The BEMT algorithm under-estimates the thrust on low rotation rates, the differential then fading until 6000 RPM. There is however good agreement between BEMT and experimental values on the torque prediction, for any rotation rate.

The probable explanation for this under-estimation of thrust at low rotation rates is an under-estimation of the coefficient of lift on low Reynolds numbers. XFOIL is difficult to use on low Reynolds numbers, and even though the calculation does converge on a value for most angles, it is even harder to reach the theoretical maximal value for the lowest Reynolds numbers (with a pitch barely lower than for the separation of the flow). The curves are then cut at a lower maximum before the high angle of attack extrapolation, probably decreasing the global lift estimation.

By using BEMT and the Hanson model, the loading noise is predicted and can be compared to the experimental acoustic measurements. As the model does not yet take into account roughness, it is tested against the wooden propeller, the experimental propeller with the lowest roughness levels. Moreover, the Hanson model only predicts the height of the tonal peaks, and these were very similar even for different propellers on Fig. 9.

The results are shown in Figures 13, 14 and 15. The Spectrum Level (SL) of the tonal noise is presented for two microphone positions in Figures 13 (4000 RPM) and 14 (6000 RPM). In both cases, the main peak (f = BPF) is accurately predicted by the Hanson model. Then, the decrease on the next peaks is larger on the model than in reality,

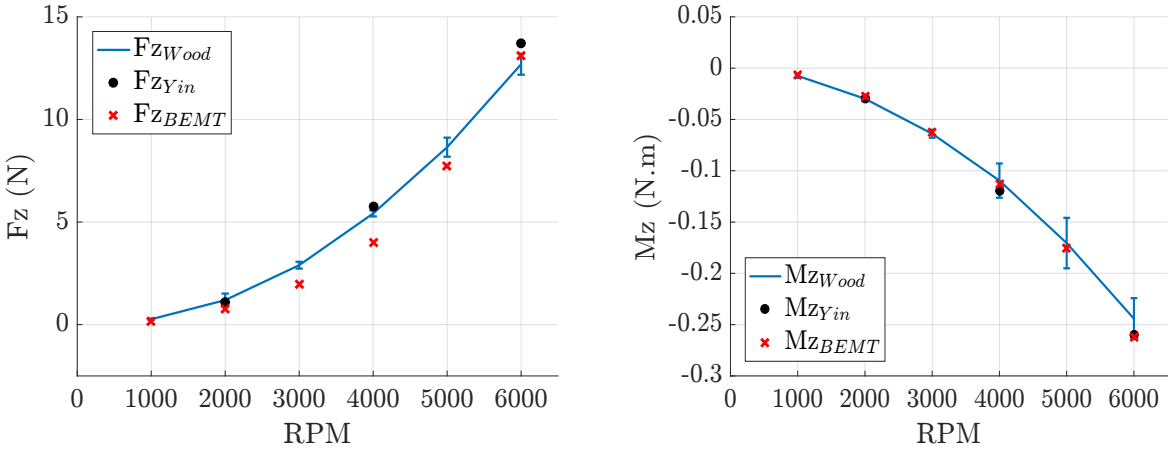

Fig. 12 Experimental measurements and model predictions of thrust and torque as a function of rotation speed and propeller. Black dots show the results of Yin et al. [9].

especially for the angle $\theta = -45°$, where the prediction becomes extremely inaccurate starting from the fourth peak.

In Fig. 15, the directivity plots show a good agreement between the model and the experimental results. The model seems less accurate the further the microphone is from the rotor plane.

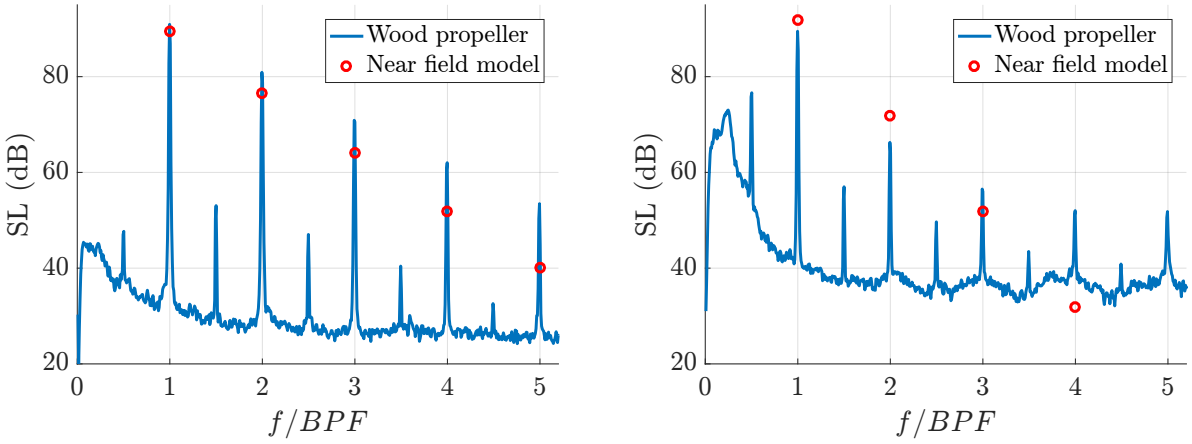

Fig. 13 Spectrum Levels (SL) for the near field loading noise model and for the wood propeller. 4000 RPM, $\theta = 0°$ on the left and $\theta = -45°$ on the right.

C. Towards an optimal roughness distribution on the blade

The presence of a laminar separation bubble on one of the boundary layers could have an important impact on the noise emitted. Such laminar separation bubbles have already been cited as responsible for broadband noise [3]. However, it is difficult to observe experimentally such a local phenomenon on a rotating propeller. The aerodynamic model can be used to investigate the presence and size of this hypothetic laminar separation bubble. The local angle of attack and induced velocity around the propeller is predicted, as was shown in Figure 5.

Then, the evolution of the boundary layer parameters along the chord can be obtained from XFOIL at different radial sections, especially the position X_{tr} of the transition of the boundary layer. This result is shown in Fig.16, for different rotation rates. On the pressure side, X_{tr} is not plotted because the boundary layer is laminar all along the chord. On the suction side, the boundary layer transitions from laminar to turbulent, at a position between $x/c = 0.35$ and $x/c = 0.6$. This transition is always occurring at the end of a laminar separation bubble (when the flow reattaches), spotted on XFOIL with negative values of C_f, the coefficient of friction on the surface. The length of the laminar separation bubble

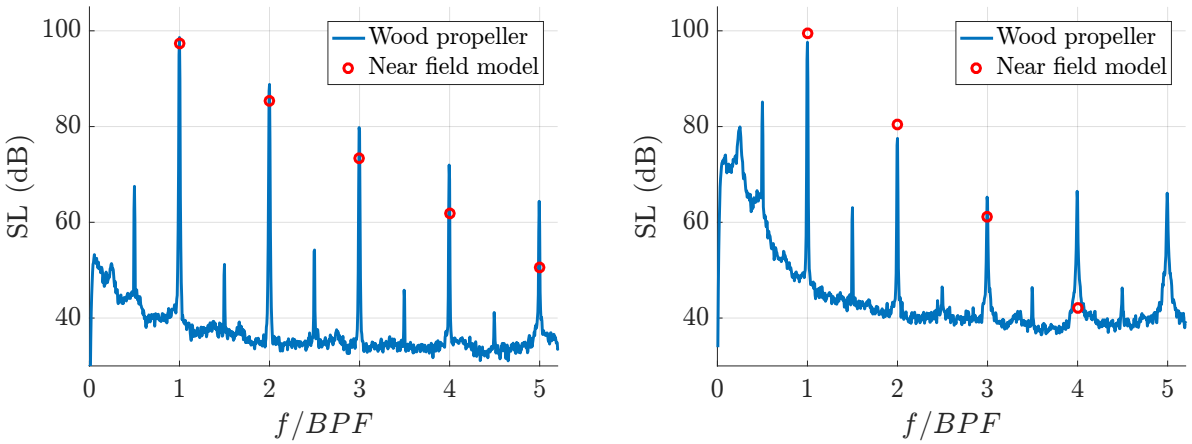

Fig. 14 Spectrum Levels (SL) for the near field loading noise model and for the wood propeller. 6000 RPM, $\theta = 0°$ on the left and $\theta = -45°$ on the right.

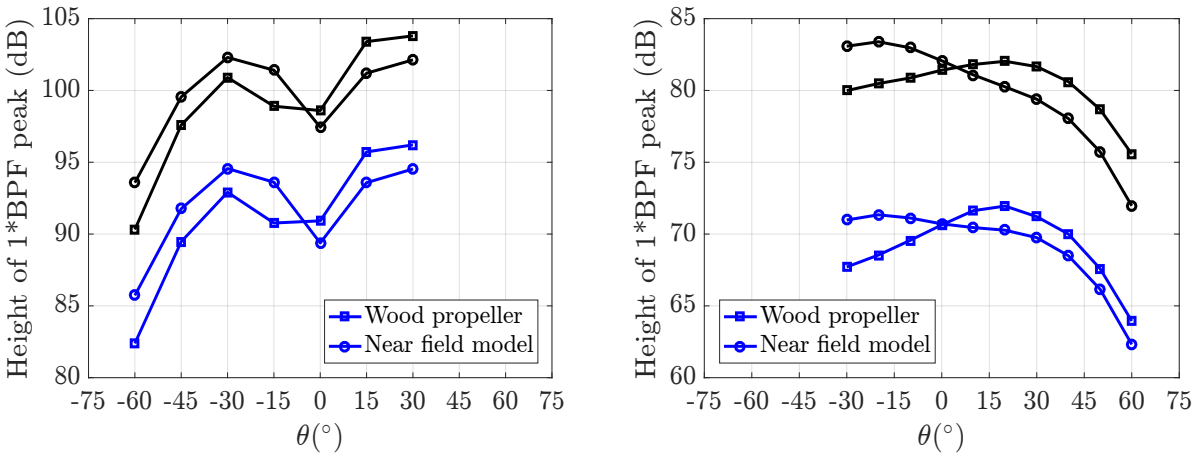

Fig. 15 Directivity figure for the near field model for loading noise, compared to the experimental measures for the wooden propeller. 4000 RPM in blue, 6000 RPM in black. R = 0.3m on the left, R = 0.7m on the right.

is plotted too. The bubble is present on the suction side for each radial position (and never on the pressure side).

IV. Conclusion and perspectives

Two different methods to approach the problem of aerodynamic and acoustic performance of low Reynolds propellers have been presented. By using both numerical models and experiments, the influence of surface rugosity on both performances is explored. Between three propellers differing on their surface rugosity, some differences appear. The PLA propeller, with the highest surface rugosity, produces a lower thrust, while the wooden propeller, with the lowest rugosity, produces more broadband noise.

This work still has lots of perspectives : first, the numerical models presented here should also soon be completed by a prediction of the broadband noise via Amiet model [12]. Moreover, the XFOIL analysis can be pushed further, either by adding a trip numerically to force the transition or by changing the parameter Ncrit (to a value of 1 instead of the standard value of 9, for example) to simulate an increase in surface rugosity. The effect of these modifications on the aerodynamic and acoustic performance of the propellers are actually being investigated.

The main idea there would be to force the transition of the boundary layer, either on the pressure side to reduce the tonal trailing-edge noise (linked to a feedback loop only possible with a laminar boundary layer [3]) or on the suction side to prevent the formation of a laminar separation bubble, potentially improving the aerodynamic properties of the

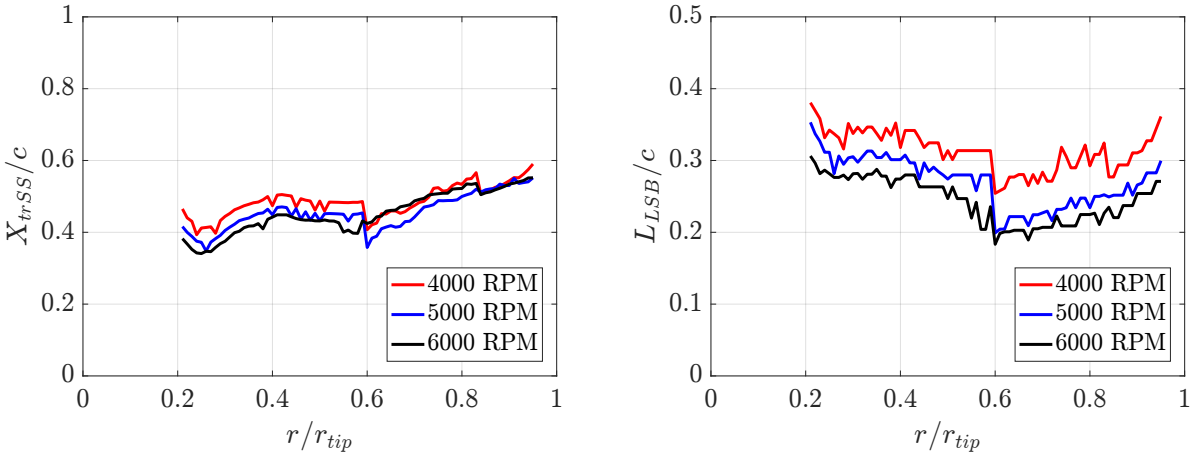

Fig. 16 Results of XFOIL analysis on the boundary layers for flow parameters obtained by BEMT : position X_{tr}/c of the transition to turbulence of the suction side's boundary layer (on the left) and length of the laminar separation bubble (on the right). Values before $r = 0.2 * r_{tip}$ and after $r = 0.95 * r_{tip}$ are ignored, as explained in part II.B.

propeller.

With this coupling of BEMT, loading noise model and XFOIL (and, in the near future, Amiet model), there is potential to design optimized blades, with controlled rugosity to change the behaviour of the boundary layers as needed and instantly compute the consequences on both aerodynamic and acoustic performances. This will allow us to propose improved propeller designs. These designs will be 3d-printed and tested in the near future.

Acknowledgments

This work was partially supported by Agence de l'Innovation de Défense - AID - via Centre Interdisciplinaire d'Etudes pour la Défense et la Sécurité - CIEDS - (project 2022 - APRO). The authors would like to thank Karl-Stéphane Rossignol and Jianping Yin from DLR for sharing their propellers and CAD, within the framework of AG26.

References

[1] Greenwood, E., Brentner, K. S., Rau, R., and Gan, Z., "Challenges and opportunities for low noise electric aircraft," *International Journal of Aeroacoustics*, 2022.

[2] Brooks, T. F., Pope, D. S., and Marcolini, M. A., "Airfoil self-noise and prediction," *NASA Reference Publication*, 1989.

[3] Yakhina, G., Roger, M., Moreau, S., Nguyen, L., and Golubev, V., "Experimental and Analytical Investigation of the Tonal Trailing-Edge Noise Radiated by Low Reynolds Number Aerofoils," 2020.

[4] Thurman, C. S., Zawodny, N. S., and Pettingill, N. A., "The Effect of Boundary Layer Character on Stochastic Rotor Blade Vortex Shedding Noise," *Vertical Flight Society's 78th Annual Forum and Technology Display*, 2022.

[5] Jaroslawski, T., Forte, M., Moschetta, J.-M., Delattre, G., and Gowree, E. R., "Characterisation of boundary layer transition over a low Reynolds number rotor," *Experimental Thermal and Fluid Science*, 2022.

[6] Ning, A., "Using Blade Element Momentum Methods with Gradient-Based Design Optimization," *Structural and Multidisciplinary Optimization*, 2021.

[7] MacNeill, R., and Verstraete, D., "Blade element momentum theory extended to model low Reynolds number propeller performance," *The Aeronautical Journal*, 2017.

[8] Hanson, D. B., and Parzych, D. J., "Theory for Noise of Propellers in Angular Inflow with Parametric Studies and Experimental Verification," *NASA Contractor Report 4499*, 1993.

[9] Yin, J., Gregorio, F. D., Rossignol, K.-S., Rottmann, L., Ceglia, G., Reboul, G., Barakos, G., Qiao, G., Muth, M., Kessler, M., Visingardi, A., Barbarino, M., Petrosino, F., Zanotti, A., Oberti, N., Galimberti, L., Bernardini, G., Poggi, C., Abergo, L., Caccia, F., Guardone, A., Testa, C., and Zaghi, S., "Acoustic and Aerodynamic Evaluation of DLR Small-scale Rotor Configurations within GARTEUR AG26," *European Rotorcraft Forum*, 2023.

[10] McCrink, M. H., and Gregory, J. W., "Blade Element Momentum Modeling of Low-Re Small UAS Electric Propulsion Systems," *33rd AIAA Applied Aerodynamics Conference*, 2015.

[11] Viterna, L. A., and Corrigan, R. D., "Fixed pitch rotor performance of large horizontal axis wind turbines," *NASA Technical Report*, 1982.

[12] Amiet, R. K., "Noise due to turbulent flow past a trailing edge," *Journal of Sound and Vibration*, 1976.